

# Advanced Nanostructured All-Waterborne Thiol-Ene/Reduced Graphene Oxide Humidity Sensors with Outstanding Selectivity

Ana Trajcheva, Justine Elgoyhen, Maryam Ehsani, Yvonne Joseph, Jadranka B. Gilev, and Radmila Tomovska\*

The current-state of polymer-based humidity sensors faces numerous limitations, including energy-costly synthesis, low sensitivity, and slow response times. This study presents innovative approach to overcome these challenges, based on a robust all-water-borne in situ miniemulsion polymerization. The use of water throughout the entire process mitigates the negative environmental impact. Thiol-ene polymers reinforced with reduced graphene oxide (rGO) with concentrations ranging from 0.2–1.0 wt% are selected to fabricate these chemoresistive sensors. The selected thiol-enes present high hydrophobicity and a semicrystalline nature, suggesting resistance to early delamination even under prolonged exposure to humidity. Incorporating rGO not only imparts electrical conductivity but also enhances mechanical and water resistance of the composite films. The 0.6% rGO composite exhibits optimal resistance for humidity sensing, demonstrating rapid and consistent responses across three exposure cycles to water vapor concentrations ranging 800–5000 ppm. Moreover, the sensor exhibits remarkable selectivity toward water vapors over these of toluene, propanol, and 4-methyl-2-pentanol, attributed to the high surface hydrophilicity and inherent porosity of the waterborne film, and network structuring of rGO platelets within the matrix. In summary, this study pioneers a novel approach to polymer-based humidity sensing, addressing key limitations while offering enhanced sensitivity, rapid response times, and superior selectivity.

numerous industrial plants such as agricultural, biomedical, meteorological, food processing, pharmaceuticals, microelectronics, etc. It is of great importance to develop humidity sensors able to monitor tiny changes in humidity; therefore, the sensor should be characterized by high sensing performance (sensitivity, selectivity, and reproducibility)<sup>[1–7]</sup> and chemical and physical stability.<sup>[2,4]</sup> In general, there are two types of humidity sensors: capacitive<sup>[5,7–9]</sup> and resistive sensors.<sup>[10–12]</sup> The mechanism of work of capacitive sensors is based on changes in the permittivity of a dielectric device. In the case of resistive humidity sensors, the working principle is based on the variation of resistance of the sensing material with humidity adsorption. Even though capacitive sensors provide better linearity in the measurements and consume less power, the resistive type is simpler, easier to use, and has the potential for miniaturization and low-cost manufacturing.<sup>[14]</sup>

A great diversity of materials has been studied for this purpose, among them ceramics,<sup>[13]</sup> polymers,<sup>[9,10,14–17]</sup> composites,<sup>[1,4,5,8,18–26]</sup> and inorganic nanomaterials.<sup>[2,3,6,11,12,7,27–29]</sup> Ceramic-, composite-, and inorganic nanomaterial-based sensors have their limitations, such as long recovery times, complex systems for water

## 1. Introduction

Atmospheric humidity is a very important parameter for evaluating the quality of the environment and is essential for

A. Trajcheva, J. Elgoyhen, R. Tomovska  
POLYMAT and Departamento de Química Aplicada  
Facultad de Ciencias Químicas  
Joxe Mari Korta zentroa  
University of the Basque Country UPV/EHU  
Tolosa etorbidea 72, Donostia-San Sebastián 20018, Spain  
E-mail: [radmila.tomovska@ehu.eus](mailto:radmila.tomovska@ehu.eus)

 The ORCID identification number(s) for the author(s) of this article can be found under <https://doi.org/10.1002/admt.202400114>

© 2024 The Author(s). Advanced Materials Technologies published by Wiley-VCH GmbH. This is an open access article under the terms of the [Creative Commons Attribution-NonCommercial](https://creativecommons.org/licenses/by-nc/4.0/) License, which permits use, distribution and reproduction in any medium, provided the original work is properly cited and is not used for commercial purposes.

DOI: 10.1002/admt.202400114

M. Ehsani, Y. Joseph  
Institute for Electronic and Sensor Materials  
Technische Universität Bergakademie Freiberg  
Freiberg Germany

J. B. Gilev  
Faculty of Technology and Metallurgy  
Ss. Cyril and Methodius University in Skopje  
Skopje 1000, R. N. Macedonia

R. Tomovska  
IKERBASQUE  
Basque Foundation for Science  
Plaza Euskadi 5, Bilbao 48009, Spain

**Table 1.** Particle size of the hybrids with 30% s.c.

Sample	Z-Ave particle size [nm]	PDI
0.0 wt% rGO	179	0.157
0.2 wt% rGO	175	0.256
0.4 wt% rGO	187	0.332
0.6 wt% rGO	182	0.331
0.8 wt% rGO	195	0.452
1.0 wt% rGO	197	0.513

desorption, limited accuracy, and the difficulty of responding to decreasing humidity levels. On the other hand, polymers received great attention due to their excellent physico-chemical properties and chemical versatility, along with their low cost, ease of use, and good sensing performance. Even though different polymer-based sensors with excellent performance have been developed,<sup>[10,30,14]</sup> the main drawback of the polymers is their low water resistance, which, at longer exposure to humid atmospheres, induces swelling and delamination of the film from the electrode.<sup>[10]</sup> Moreover, the proposed synthesis methods for this type of sensing material are based on solvents,<sup>[10,14,31]</sup> or they require costly equipment,<sup>[30]</sup> which may limit their practical application potential.

A recent review study reported by Ehsani et al.<sup>[32]</sup> summarizes the significance of composites based on nanocarbon/polymer combinations for chemiresistive sensing, in which the nanofiller enables conductivity while the polymer provides adsorption affinity. Polyamides, polyamines, polymethacrylate, polystyrene, and polyvinyl alcohol reinforced with GO and rGO are among the most commonly used nanocarbon/polymer composites. In order to be considered good chemiresistor sensing materials, these composites have to fulfil the criteria of homogeneous distribution of nanofiller within the polymer to allow a reproducible design of a percolation pathway. Various polymer/nanocarbon composites have been deeply investigated as humidity sensors, and some researchers have demonstrated their potential and high perfor-

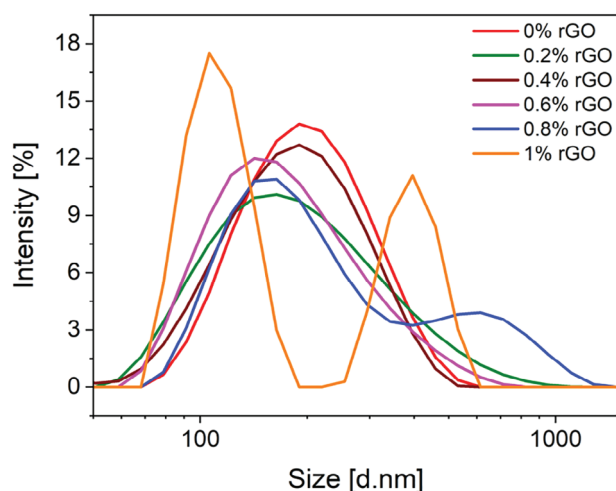


**Figure 1.** Particle size distributions of neat polymer and hybrid latexes containing different rGO quantities.

mance ability in terms of good stability<sup>[2,13]</sup> and sensitivity.<sup>[5,26,7,6]</sup> However, these composite materials possess important challenges, such as slow response time and limited detection range, along with the fact that high nanocarbon filler loading in the polymer matrix is necessary for good performance, which might increase the cost of the final products.

As a response to the presented challenges of the current humidity sensors, in this work we have developed novel humidity sensors, based on waterborne nanocomposites made of thiol-ene polymers and small quantity of rGO. The composites are synthesized via in situ miniemulsion polymerization, in which composite particles made of thiol-ene polymer and rGO nanoplatelets are predominantly created by the nucleation of the preformed thiol-ene monomer droplets dispersed in water. Miniemulsion is a kinetically stable colloid system in which monomer droplets in the submicron range are dispersed in water. The coalescence of the droplets is prevented by the presence of surfactants, whereas diffusional degradation of the monomer droplets (Ostwald ripening) is avoided by the addition of co-stabilizers, usually low-molar-mass highly hydrophobic compounds. Organized in this way, it is ensured that during polymerization each composite particle will have the same composition, which is especially useful when several different material types are combined within one droplet or particle (in this case, dithiol, diene, and rGO).<sup>[33,34]</sup> After polymerization, the monomer droplets are turned into polymer particles dispersed in water.<sup>[35]</sup> rGO platelets are preferably distributed on the surface of the particles.<sup>[34,36]</sup> Miniemulsion polymerization is an environmentally friendly technique because of the use of water as a continuous phase and polymerization medium. Moreover, after composite film preparation by water evaporation from the aqueous dispersions, the aggregation of rGO platelets within the polymer matrix is suppressed because the rGO platelets are placed in-between the polymer particles that physically hinder the platelet aggregation.<sup>[10]</sup>

The key challenge for the development of an efficient polymer-based humidity sensor is to find a compromise between high affinity to adsorb water on the surface of the sensing material, which is necessary for good sensing ability, and being hydrophobic enough to avoid early lamination and sensor degradation. This issue requires a careful search for novel chemistry polymers that have not been used yet in sensing applications. Thiol-ene chemistry is a well-known polymer chemistry that has sparked new interest for different applications because of its numerous advantages. Through step-growth radical polymerization, they form polymers with high monomer conversions, low shrinkage, little oxygen inhibition, and homogeneity in mechanical properties.<sup>[37–39]</sup> With proper selection of the chemical structure, thiol-ene polymers can be highly hydrophobic and semicrystalline; while simultaneously the presence of S heteroatoms, carbonyl groups, and ether functional groups will promote humidity adsorption due to the possible formation of hydrogen bonds with water molecules. As it was already mentioned, most of the polymers tend to delaminate from surfaces when they are exposed to a humid atmosphere for a long period of time due to the swelling effect. Thiol-enes, on the other hand, can withstand in high humidity atmosphere when highly hydrophobic and semicrystalline, which provide a strong barrier to the penetration of humidity within the polymer.<sup>[40,41]</sup> Up to the best of

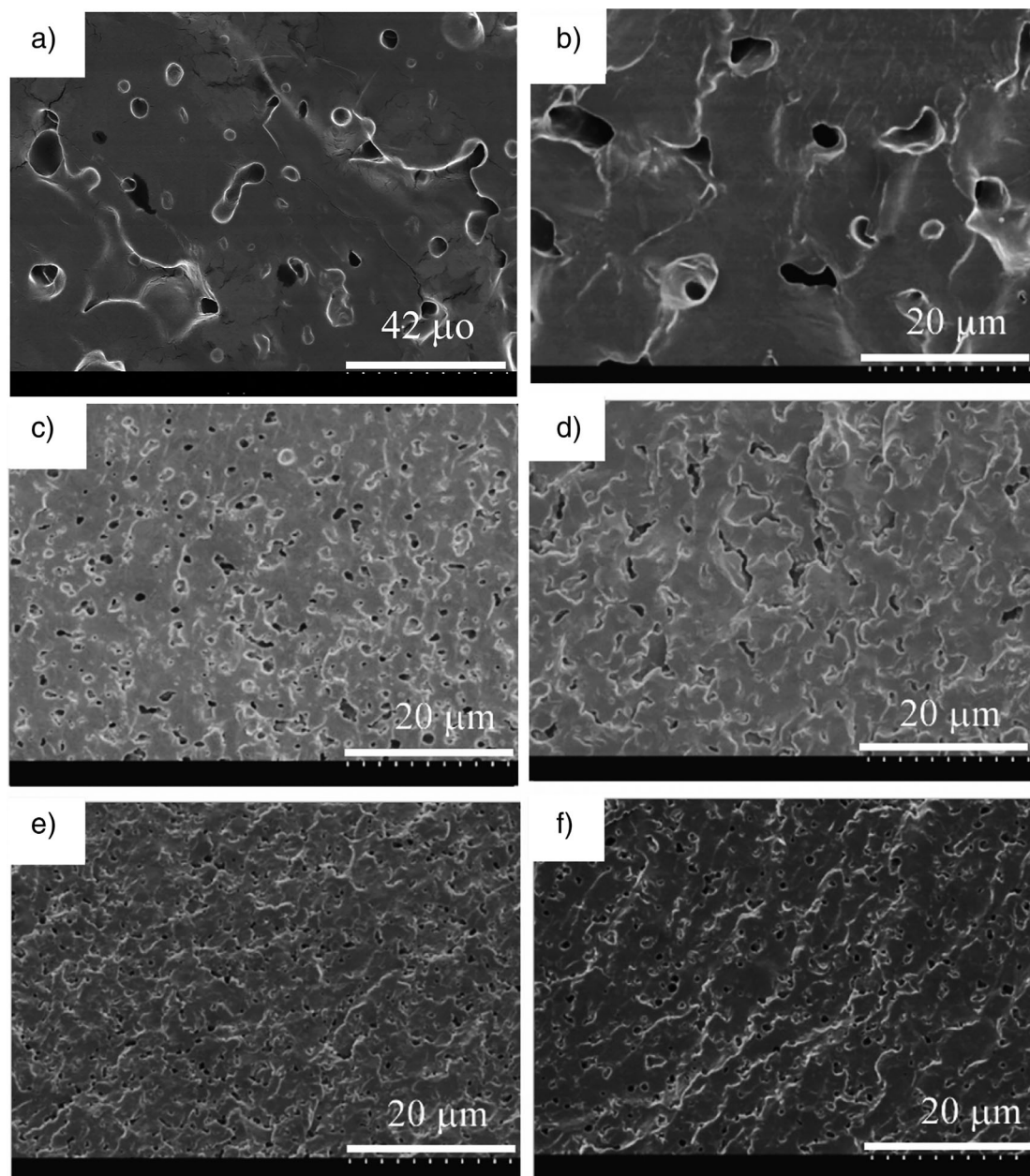


**Figure 2.** SEM cross-sectional images of the samples with: a) 0 wt% rGO; b) 0.2 wt% rGO; c) 0.4 wt% rGO; d) 0.6 wt% rGO; e) 0.8 wt% rGO; f) 1 wt% rGO.

the authors' knowledge, so far, the thiol-ene polymer system has not been investigated for humidity sensor application.

Furthermore, the loading of rGO into the polymer matrix will provide robustness and physical stability, as well as the required conducting network since a resistive-type humidity sensor was targeted. Due to the highly linked network created between rGO and the thiol-ene polymer and the semi-crystalline nature of the polymer matrix, the physical stability upon exposure to humidity can be ensured. Moreover, the rGO-thiol-ene interface offers additional adsorption sites for the water molecules, which can result in increased humidity detection of the sensor material.

## 2. Results and Discussion

### 2.1. Characteristics of the Polymer/rGO Composites

To synthesize polymer/rGO nanocomposites, in situ miniemulsion was implemented, resulting in a range of composite latexes (aqueous dispersions of polymer and rGO particles) with a rGO load of 0.2–1.0 wt%. The average particle sizes of the latexes, ranging from 179 to 197 nm, are shown in **Table 1**. As previously demonstrated,<sup>[34,36]</sup> likely the composite particles were generated during the in situ reaction, in which thiol functionality may establish H-bond with OH or COOH from rGO. Moreover, trithiol

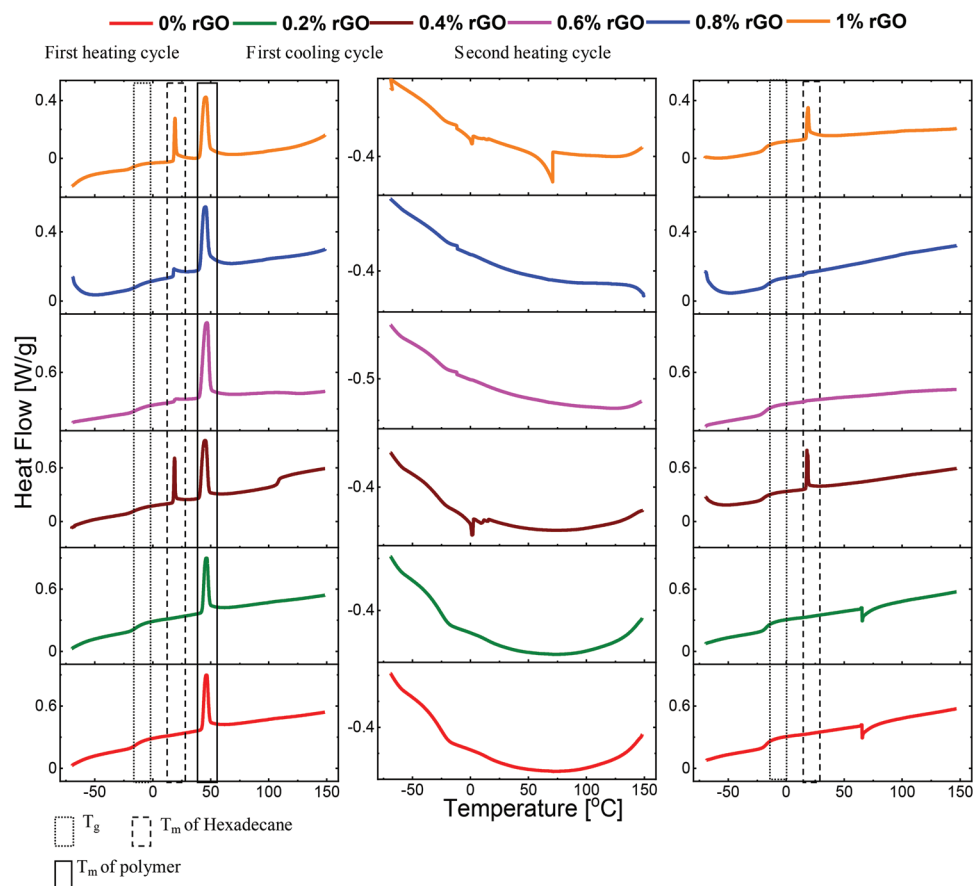


Figure 3. DSC results of the nanocomposites.

was also used during the thiol-ene synthesis, which implies the formation of a cross-linked structure.

Polydispersity (PDI) increases with the addition of rGO and the increase in its content, indicating a wide size distribution of particles. In Figure 1, the particle size distributions corresponding to each dispersion are presented, illustrating this trend. The loading of rGO substantially influences it, causing a slight shift toward lower molar masses. For the highest loadings (0.8% and 1.0% rGO), the distributions become bimodal. This behavior suggests secondary nucleation occurring in the system, likely promoted by the presence of rGO. Despite the particles being stabilized against aggregation by the surfactant (Dawfax A1) in the miniemulsion system and against Ostwald ripening by the co-stabilizer (hexadecane), it appears that monomer diffusion occurred, leading to polymerization in the aqueous phase and the nucleation of new particles. This implies the presence of two types of particles in the system: two-phase particles (rGO/polymer) produced by droplet nucleation and single-phase particles (polymer) nucleated by homogeneous nucleation.

The dispersions were cast in silicon molds and dried at standard atmospheric conditions (23 °C and 55% relative humidity). During this process, while water is evaporating, the composite particles are packed together. The low  $T_g$  of thiol-ene polymer chains in an expected range of  $-18$  to  $-20$  °C<sup>[42]</sup> allows their interdiffusion through the particle-particle

boundaries, creating a continuous film. Figure 2 presents the Scanning Electron Microscopy (SEM) images of the composite films' cross-section at different rGO loadings, showing that all the films have similar morphology in which the graphene sheets (whitish structures) are randomly oriented with no aggregation within the polymer matrix (dark grey or black). Unexpectedly, a presence of pores with a diameter in a range of 1 to 10  $\mu\text{m}$  can be observed in the images of all the films, including in the neat polymer film.

Pores can be formed either due to incompatibility between the two phases or due to the crystallization of the polymer chains.<sup>[43]</sup> It is well known that linear thiol-ene polymer chains are prone to crystallization,<sup>[37–41]</sup> which during film formation are stacked sequentially in an ordered pattern, resulting in the formation of crystalline structures in an amorphous matrix. The formation of the pores can be attributed to this phenomenon. Furthermore, by increasing the rGO loading (Figure 2b–f), the size of the pores decreases, as does the size of the polymer domains, indicating that the rGO presence affects the structuring. There are three phases within the composite films: rGO-polymer hybrids, neat amorphous polymers, and neat crystalline polymers. Therefore, the phase separation between the phases is likely also an important tool toward the creation of small pores. Similar morphology has been observed and reported previously,<sup>[44]</sup> in methyl methacrylate/methyl acrylate waterborne films, in which

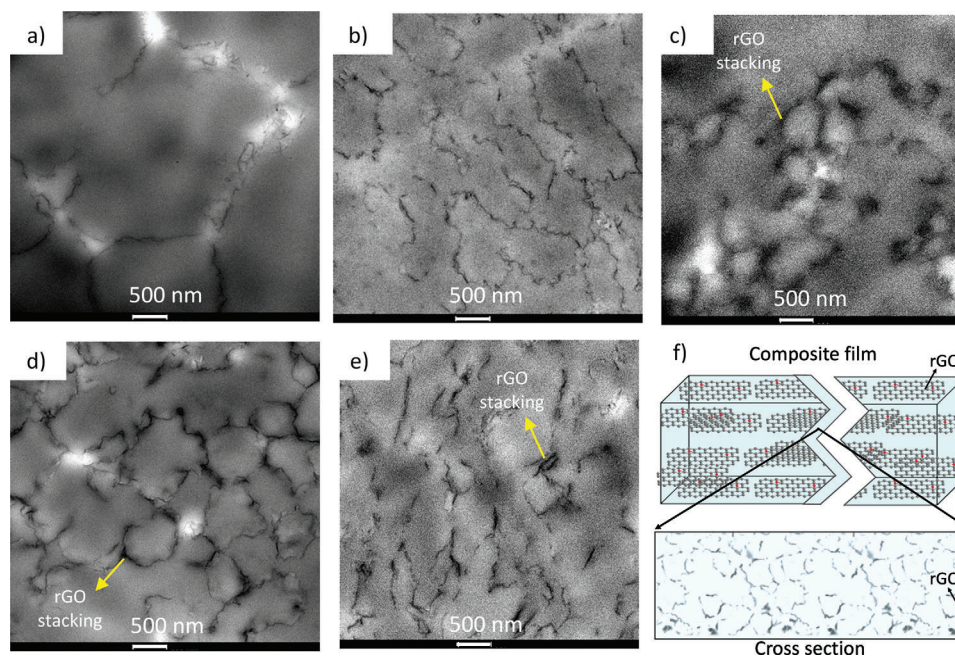


**Figure 4.** Cross-section TEM images of the composite films containing: a) 0.2 wt% rGO; b) 0.4 wt% rGO; c) 0.6 wt% rGO; d) 0.8 wt% rGO; e) 1.0 wt% rGO, f) scheme of rGO distribution in the polymer matrix.

the pores were created after film immersion in water. This phenomenon was explained by water phase separated domains. Nevertheless, in the present case, the pores were formed during film formation, without exposure of the films to water afterward. By increasing the rGO loading, the rGO-polymer phase quantity is also increased, which contributes to decreasing the size of the pores and increasing their quantity. These pores might offer an additional surface for vapour adsorption and can promote fast response and recovery times by changing the diffusion behaviour.

The previous work has shown that the thiol-ene polymers used in this study have a crystallinity in the range of 25–45%.<sup>[45]</sup> The semi-crystalline behavior of as-synthesized films is evidenced by the presence of an endothermic melting peak at  $\approx 41$  °C in the first heating scans of non-isothermal differential scanning calorimetry (DSC) analysis, shown in Figure 3.

When the rGO loading is  $>0.2$  wt%, there is a second melting peak observed in the first heating scan at 18 °C, attributed to the melting of hexadecane, used during the synthesis of the latexes as a co-stabilizer to prevent the Ostwald ripening process. As it is not volatile, it becomes distributed throughout all films. The presence of this second melting peak reveals that in the samples containing rGO  $>0.2$  wt%, hexadecane segregates from the polymer matrix, likely due to the decreased compatibility of HD with the rGO-polymer phase. In Figure 3, it can also be observed that when the films were cooled down from their molten state at  $10$  °C  $\text{min}^{-1}$ , no recrystallization peak was observed in the DSC scans, attesting slow-crystallising material. This is likely due to the presence of aromatic rings in the thiol-ene chains of diallyl terephthalate (DATP) ene, which add rigidity to the chains and slow down their ordering in crystalline domains. Consequently, no melting peak attributed to the polymer matrix is present in the subsequent heating scan at  $10$  °C  $\text{min}^{-1}$ . In this last run, the

glass transition temperature ( $T_g$ ) of the material could be appreciated at  $-9$  °C. Noteworthy, the  $T_g$  and melting temperature ( $T_m$ ) of the polymer were surprisingly unaffected by the presence of rGO platelets within the matrix (Table 2), which is an indication that there is only physical interaction between the polymer and rGO platelets. It is worth noting that the creation of the crystalline structure during water evaporation and composite film formation, observed in the first heating scan, will provide the composite film with higher durability and less water sensitivity, preventing early lamination of the sensors.

To investigate the nanocomposites' structure, Transmission Electron Microscopy (TEM) analysis of the cross section of the films was conducted, and the resulting images are depicted in Figure 4. The dark structures corresponding to rGO sheets are embedded within the light grey polymer matrix. In all composites, no rGO aggregation is noticed, but the platelets form a network within the polymer matrix. The graphene platelets are very well ordered perpendicularly to the film cross-section or parallel to the top film surface, as shown in Figure 4f. The ordering is induced by the slow water evaporation during the film formation, during which the platelets are pushed between the polymer layers created by the particle fusion. The low  $T_g$  (Table 2) permits particle fusion at room temperature by the chain interdiffusion process across the particle border. Another phenomenon that can be observed is the stacking of the graphene platelets, which is a common phenomenon for graphene-based nanocomposite. This is due, in part, to the weak Van der Waals interactions between graphene sheets, which allow them to readily slide or align with one another, resulting in the formation of multilayered structures. When the concentration of graphene increases, graphene sheets are more likely to come into close contact and stack. That is why, for concentrations  $>0.6$  wt%, the stacking of

**Table 2.**  $T_g$  and  $T_m$  of the nanocomposites.

Sample	First heating cycle			Second heating cycle		
	$T_g$ [°C]	$T_m$ Hexadecane [°C]	$T_m$ polymer [°C]	$T_g$ [°C]	$T_m$ Hexadecane [°C]	$T_m$ polymer [°C]
0.0 wt% rGO	−8	−	41	−8	−	−
0.2 wt% rGO	−9	−	41	−10	−	−
0.4 wt% rGO	−10	18	43	−10	18	−
0.6 wt% rGO	−8	18	41	−9	−	−
0.8 wt% rGO	−8	18	41	−8	18	−
1.0 wt% rGO	−10	18	42	−9	19	−

graphene can be observed in Figure 4c–e as thicker platelets, thus darker structures. Figure 4f provides a schematic illustration of the nanocomposites cross section and almost ideal distribution of rGO sheets.

Even though the samples have a porous structure, which resulted in a high standard deviation in the elongation at break, the measurements were reproducible under low stress, from which the Young's moduli and offset yield stress were determined, shown in Table 3. The introduction of rGO in the polymer matrix resulted in enhanced properties; thus, at 1.0 wt% rGO loading, fourfold higher Young's modulus was observed with respect to the neat polymer. The yield stress results do not show any significant trend. The improvement of Young's moduli suggests very good interactions between both phases within the nanocomposites, which accounts for the good stress transfer when the composite films are exposed to stress. As already highlighted, the thiol functionality might interact with OH or COOH from rGO through H-bond creation during in situ synthesis. Therefore, nanocomposites are distinguished by their higher strength as they can withstand higher levels of stress without undergoing plastic deformation.

One of the most important challenges related to the use of polymers as humidity sensors is their tendency to swell in humid atmospheres, which causes delamination from the substrate.<sup>[10]</sup> Even though thiol-ene polymers are known for their low water uptake properties, in the case of waterborne thiol-ene polymers, the use of surfactant for their preparation usually negatively affects their water sensitivity. Water uptake measurements for the neat polymer and the composites were carried out for a duration of 21 days by dipping the films in water dur-

**Table 3.** Young's modulus and Offset Yield Stress for the obtained composites.

Sample	Young's Modulus [MPa]	Offset Yield Stress [MPa]
0.0 wt% rGO	0.01	0.01±0.005
0.2 wt% rGO	0.01	0.02±0.001
0.4 wt% rGO	0.02±0.005	0.01
0.6 wt% rGO	0.03	0.01±0.005
0.8 wt% rGO	0.03±0.005	0.02±0.005
1.0 wt% rGO	0.04±0.005	0.02±0.005

ing different period of times, and the results are placed in Figure 5. Even though the neat polymer already presents low water uptake, < 11%, at which a kind of saturation is achieved, the addition of rGO further improves the water resistance of the films. The small decrease in water uptake observed in some of the films likely corresponds to the dissolution of water-soluble components (surfactants) from the films into water. The composite film loaded with 1.0 wt% rGO absorbs only ≈2% water, which is ≈fivefold lower than that of the neat polymer film. The exceptional water resistance of these composites may be attributed to the interplay of several characteristics. Thiol-ene polymers are highly hydrophobic and contain crystalline domains, while rGO platelets are strongly bonded to the polymer chains, enhancing further the hydrophobicity. The physical barrier created by the network of rGO on one hand and the crystalline thiol-ene structure on the other restricts water absorption, leading to enhanced water resistance. It is worth mentioning that after 24 days of immersion of water, there was no any delamination observed of the polymer and composite films.

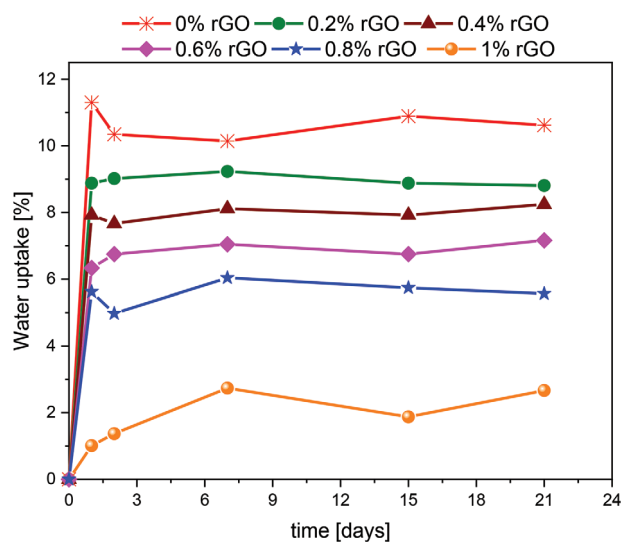


**Figure 5.** Water uptake by the neat polymer and composite films containing different rGO loadings.

**Table 4.** Resistance of nanocomposites.

Sample	Resistance k $\Omega$
0.0 wt% rGO	—
0.2 wt% rGO	48.5
0.4 wt% rGO	700
0.6 wt% rGO	7200
0.8 wt% rGO	5600
1.0 wt% rGO	4400

## 2.2. Sensor Performance

For humidity sensing measurements, a handcrafted chemical resistance sensor was employed. The resistance of the resulting composites was therefore tested, and the results are given in **Table 4**. The nanocomposite containing 0.2 wt% rGO is the most conductive which is an indication that completely interconnected network of rGO is formed within the matrix. Further increase in rGO loading increase the resistance, likely due to re-stacking of the rGO platelets during the synthesis process at higher rGO loadings. Moreover, as the network of rGO is denser at higher concentration, there is a possibility that the network is not completely interconnected, but rather is interrupted with neat polymer areas. The rGO re-stacking might clearly be observed in the composites with rGO loadings >0.6 wt% in **Figure 4c–e**. When the rGO loading is augmented, two contradictory effects happen, there is more rGO to form the conductive network and increase the conductivity, but also the possibility for rGO stacking increase that might decrease the conductivity. When the loading was increased from 0.2 to 0.6 wt%, the effect of graphene stacking was likely higher than the loading effect, leading to increased resistance. By further increasing rGO loading up to 1.0 wt%, the loading effect becomes higher because of the very high surface area and aspect ratio of the rGO nanoplatelets. Therefore, for the nanocomposites containing 0.8 and 1.0 wt% rGO, the resistance

**Table 5.** Water vapor adsorption and desorption results at different concentration by the nanocomposite containing 0.6 wt% rGO.

Ppm	Adsorption			Desorption		
	$\Delta R$ [%]	Time $t_{100}$ [s]	Time $t_{90}$ [s]	$\Delta R$ [%]	Time $t_{100}$ [s]	Time $t_{90}$ [s]
800	3	13 $\pm$ 3	11.7 $\pm$ 3	3 $\pm$ 1	19 $\pm$ 6	17 $\pm$ 6
1600	6	11 $\pm$ 1	9.9 $\pm$ 1	5	19	17.1
3200	14	17 $\pm$ 2	15.3 $\pm$ 2	13 $\pm$ 1	35 $\pm$ 1	31.5 $\pm$ 1
5000	26 $\pm$ 1	20 $\pm$ 0.5	18 $\pm$ 0.5	25 $\pm$ 2	30 $\pm$ 3	27 $\pm$ 3

drops with respect to the 0.6 wt% loading, even though it is much higher than that of 0.2 and 0.4 wt% filler loadings.

All the nanocomposites were deposited as a thin film for sensing measurements and were exposed to humidity. However, only 0.6 wt% nanocomposite has shown to be sensible to humidity, likely due to the highest resistance of this composite film, therefore it was further studied. Probably, the threshold resistance for humidity sensing of the present nanocomposites would be in-between 5600 and 7200 k $\Omega$ . Moreover, the resistance of the nanocomposite increased upon exposing it to humidity. Considering that rGO is p-type material, in contact with water molecules that have reducing characteristics, the concentration of the charge carriers (holes in this case) decreases inducing a rise of the resistance.

The sensing performance of the 0.6 wt% composite was investigated in terms of resistance change ( $\Delta R$ ) when the composite was exposed to different concentrations in a range of 100–5000 ppm of water vapor at room temperature. To check the reproducibility, each concentration of vapor was run in three cycles. The  $\Delta R$ , as well as the time required for that change to occur during the vapor adsorption and desorption cycles were considered indicators of sensing performance. The effect of the concentration of water vapor on the sensing performance of the 0.6 wt% composite is shown in **Figure 6**, showing sensing properties and stable response for vapor concentrations higher than 800 ppm.

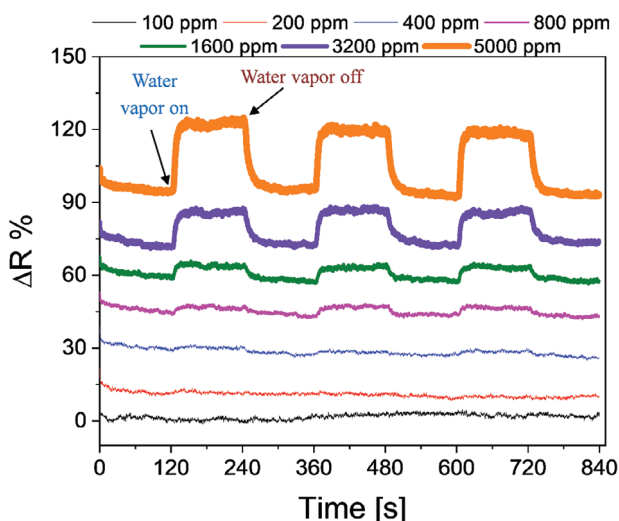


**Figure 6.** Sensor response of 0.6 wt% rGO nanocomposite toward water vapor.

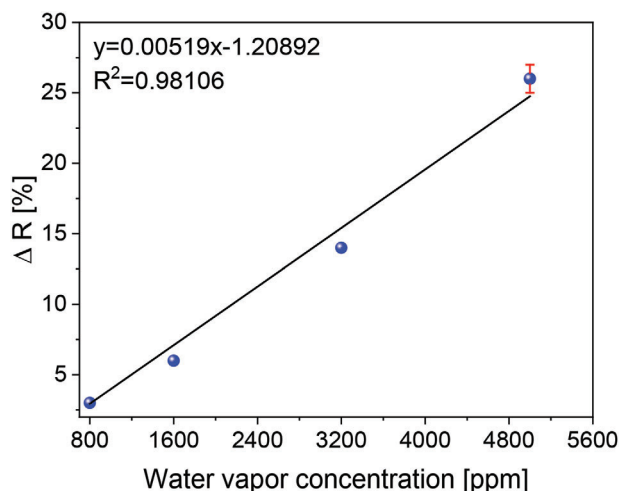


**Figure 7.** Water vapor concentration-dependent response of 0.6 wt% rGO nanocomposite: a linear fit analysis.

The obtained responses presented in Figure 6 have almost an ideal sensor pattern, and a linear fit curve shown in Figure 7 can precisely describe the relation between water vapor concentration and the response. Table 5 summarizes the sensing parameters determined from Figure 6, the sensing response ( $\Delta R$ ) and the time it takes for the sensor to reach 100% ( $t_{100}$ ) and 90% ( $t_{90}$ ) of its final response. As water molecules are absorbed, the resistance is increased up to  $26\% \pm 1\%$  for a water concentration of 5000 ppm, and a stable response ( $t_{100}$ ) is achieved in  $20 \text{ s} \pm 0.5 \text{ s}$ . The time required for the sensor to reach 90% (23.4% resistance increment) of the final concentration ( $t_{90}$ ) is  $18 \text{ s} \pm 0.5 \text{ s}$  (Table 5). The difference between  $t_{90}$  and  $t_{100}$  is not significant, and this indicates that the sensor can provide both a fast initial response and a quick stabilization. This can be particularly beneficial in scenarios where frequent changes in humidity occur or where precise and real-time monitoring is necessary. In comparison to other humidity sensors, this particular sorbent material exhibits a relatively good and fast response. On the other hand, the desorption took a longer time ( $30 \text{ s} \pm 3.2 \text{ s}$ ), and the change in resistance was  $24.8\% \pm 2.4\%$ . The resistance did not return to its exact original value (Table 5); this can indicate that maybe some of the water molecules interacted in a more stable way with the sensing material. The diffusion of vapor molecules is influenced by film structural parameters such as thickness and porosity.<sup>[46]</sup> The porous structure of the films, as evidenced by the SEM images in Figure 2, has a positive contribution to the diffusion process of the water molecules inside the composite film, even though the desorption was not 100% complete and was slower.

Aside from sensitivity and fast response, reproducibility is perhaps the most critical parameter for a chemical sensor. The reproducibility was investigated in 3 cycles, and as it can be seen from Figure 6 as well as from Table 5, the nanocomposite with 0.6 wt% rGO showed reproducible behavior, where there is no variation between the signals or the variations are very modest.

Selectivity of the sensor to respond only to water vapor while minimizing responses to other substances was also studied. For that aim, the composite containing 0.6 wt% rGO was exposed to various non-polar and polar solvents' vapors (toluene, propanol, and 4-methyl-2-pentanol (4M2P) at room temperature at a concentration of 5000 ppm (the highest studied in this work). Figure 8 denotes the responses of the composite to the vapors of the selected solvents in comparison to that of water. At 5000 ppm humidity concentration, while there is almost no signal of sensing of the solvents' vapors, the signal to water vapor is clear, strong, and reproducible, as previously commented. The results shown in Figure 8 actually indicate specific chemical interaction of the nanocomposite with the humidity, that is not observed for the other vapors. Such specific interactions cannot be provided by rGO platelets, because of high adsorption ability of rGO and the fact that any type of reduction gas would induce resistivity rise. Considering the morphology of the composite materials observed in Figure 2, the rGO platelets are embedded within the polymer matrix, therefore, the polymer phase is the one in direct contact with the vapors. The composite has shown strong affinity toward humidity, likely due to the presence of S— and O— based ( $\text{C}=\text{O}$ ,  $\text{C}-\text{O}-\text{C}$ ) hydrophilic moieties in the polymer, allowing suitable interactions with water molecules through formation of hydrogen bonds. Additionally, treating with waterborne polymers, during film formation from the polymer aqueous

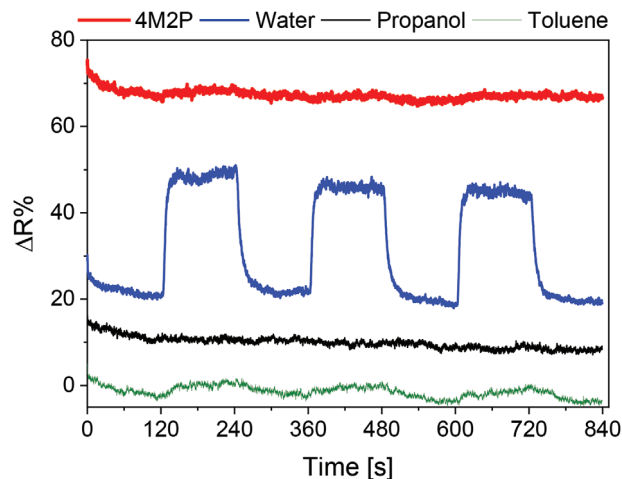
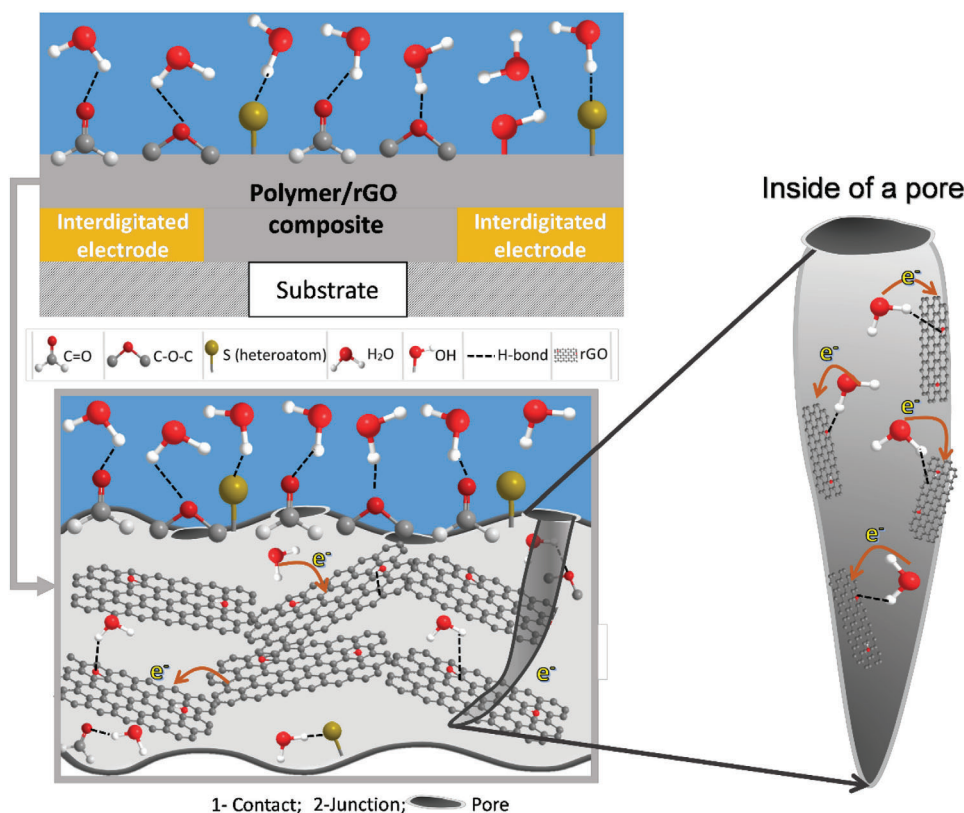


Figure 8. Sensor response of 0.6 wt% rGO nanocomposite to 5000 ppm of 4M2P, water, propanol, and toluene.

dispersion, the surfactant used to ensure colloidal stability during synthesis and storage, migrates toward the film surfaces. This makes the surface of the film much more hydrophilic and able to interact principally with water molecules. The fact that after exposure to humidity the resistance increased indicates that there is a direct contact of the absorbed humidity with rGO platelets, too. The presence of the pores in the composite (Figure 2) allows deeper penetration of the humidity and makes possible interactions with the rGO or more likely with the rGO/polymer interface. It seems that the exceptional nanostructuring that happen during water evaporation from the polymeric dispersions and composite film formation, in which highly hydrophilic surface onto very hydrophobic bulk composite materials, moreover porous and with a network of rGO platelets within the matrix, unlock their humidity sensing properties and application.

On the other hand, the composite shows very low or no affinity toward the other vapors studied. Main reason for lack of the interaction of the mentioned vapors with the present composite is the presence of surfactant on the composite surface that preferably interacts with water molecules. Nevertheless, there are issues that might additional affect negatively the ability to interact with the nanocomposite. Propanol possesses an OH functional group that can eventually establish hydrogen bonds with the  $\text{C}=\text{O}$ ,  $\text{C}-\text{O}-\text{C}$ , and the heteroatom S from the polymer surface, but it has a lower dipole moment (1.65 Debye) than water (1.84 Debye), making weaker the interactions, but also the larger molecular size would make more difficult the permeation. On the other hand, 4M2P has a greater 2.69 D dipole moment, however, the lack of H-donor moieties, making its interactions with the polymer weaker, and similarly it has larger molecular size that affects negatively to permeate the polymer matrix and reach the rGO functional groups. Finally, toluene is aromatic solvent compatible with rGO and could easily interact with the platelets. Nevertheless, likely toluene vapors do not get in contact with platelets embedded within the polymer matrix, due to lack of H-bonding potential and polarity. Toluene vapors are not absorbed by the polymer and do not penetrate within the pores, resulting in the lack of sensing response when the composite is exposed to toluene vapors.



**Figure 9.** Schematic representation of the humidity sensing mechanism of 0.6% rGO nanocomposite.

**Figure 9** provides a schematic representation to illustrate the sensing mechanism of the composite-based interdigitated humidity sensor. The sensing starts with abundant adsorption of water vapor molecules on the surface of the composite largely assisted by the presence of surfactant on the surface, followed by absorption of these molecules within the composite material. The presence of pores in the structure contributes essentially in the humidity absorption. This means that the primary interactions occurred between polymer and water molecules, which actually determines the selectivity of the sensor. Once penetrated within the composites, the water molecules preferably stack to the rGO/polymer interface, as a key event that induces the sensing response. rGO network within the polymer matrix (Figure 4), determines the initial resistance, which after interaction with humidity increased. As p-type material, the conductivity of rGO is determined by the excess of holes, the concentration of which is higher than that of free electrons. After interaction with humidity molecules that behave as free-electron donors, reducing the holes and increasing the film resistance happen, as visualized in Figure 9. Moreover, the presence of water vapor might induce swelling within the composite, causing an increase in the intersheet distance. As a result, the hopping distance for electrons is increased, leading to difficulties in electron transfer and additional increase in the composite resistance. The effect of swelling caused by adsorbed water is particularly noteworthy when the sensor is exposed to high water vapor concentrations. At higher concentrations, more water molecules permeate the composite and are adsorbed on the interface between the polymer

and the graphene sheets. Consequently, the sensor resistance increases substantially. The importance of the water vapor concentration was already demonstrated (Figures 6 and 7), where above 800 ppm, the swelling had an effect on the disturbance of the conductive rGO path within the polymer. During the water desorption from the composite, a shrinkage effect and reconstruction of the electron conductive path are taking place, resulting in a decrease in the sensor resistance.

### 3. Conclusion

The in situ green miniemulsion polymerization process was used to make waterborne thiol-ene composite materials based on rGO nanoplatelets. Colloidally stable, film-forming, high-solids-content hybrid latexes were developed using monomer mixture made of DATP/GDMA/TMPMP with different rGO loadings of 0.2, 0.4, 0.6, 0.8, and 1.0 wt%. Composite films were produced by water evaporation, during which structuration is achieved on nano and microlevel, as observed by SEM and TEM. The nanoplatelets created a network within the polymer matrix using the polymer particles as a template for it. Beside the low  $T_g$  of  $\approx -8$  °C, nice composite films were obtained due to semi-crystalline nature of the thiol-ene, which moreover contributed to development of pores.

The mechanical characteristics of the nanocomposites were greatly influenced by the addition of rGO. Despite the porous structure of the samples, which resulted in a significant standard deviation in elongation, when 1.0 wt% of rGO was introduced,

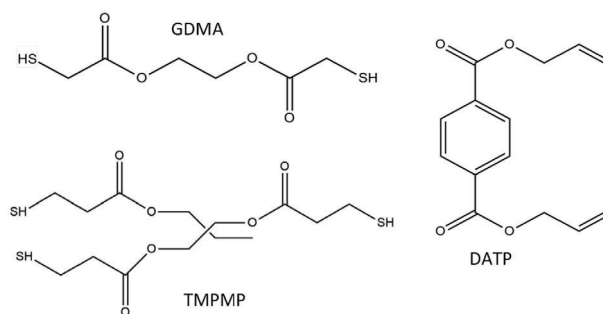
the increase in Young's modulus was fourfold with respect to the neat polymer film. The introduction of rGO platelets dropped the water uptake of the composite films with respect to neat polymer film, upon their immersion in water. Likely the distribution of the platelets parallel to the film's surfaces created a barrier to water absorption. The highly hydrophobic and semi-crystalline nature of the film contributes to lack of any delamination of the composite materials during extended immersion in water. The composite films present resistance in a range of 48–7200 k $\Omega$ , likely result on the creation of the rGO network within the film.

Only the composite containing 0.6 wt.% rGO has shown sensing affinity toward humidity, likely due to the highest resistivity encountered for this composite. This composite was exposed to humidity with various water vapor concentration (100–5000 ppm) at ambient temperature. For concentrations above 800 ppm, there was almost an ideal square-shaped response. When exposed to 5000 ppm of water vapor, the composite exhibited a comparatively good ( $26\% \pm 1\%$  resistance increase) and rapid ( $t_{100} = 20 \text{ s} \pm 0.5 \text{ s}$ ) response. Desorption took ( $t_{100}$ ) =  $30 \text{ s} \pm 3 \text{ s}$  and resulted in a  $25\% \pm 2\%$  change in resistance. The resistance did not recover to its initial value, which could imply that some of the water molecules were linked to the sensing material in more stable form, nevertheless this did not affect the sensing capacity of in next cycle. In three cycles of exposure to each humidity concentration, excellent reproducibility of the sensing response was achieved. The composite exhibited high selectivity to water vapors, while there was no any response to vapors of toluene, propanol, or 4M2P. The strong selectivity observed was attributed to the chemistry of the thiolene polymer matrix produced in aqueous dispersion, which convey to the films strong hydrophilic character of the composite surface on contrary to the strong hydrophobic and semicrystalline nature of the matrix. The porous nature allows penetration of the adsorbed water molecules within the film and their interaction with rGO. During this interaction the resistance of the composite film increased due to reduction of the holes within the p-type rGO platelets, which process unlocked the sensing characteristics of the nanocomposite.

Separately from their selectivity, reproducibility, and fast response, the proposed sorbent materials have significant advantages such as low cost, a simple, environmentally friendly manufacturing process, ease of use, and a good withstand of water uptake, making them suitable for use as humidity sensor materials.

## 4. Experimental Section

**Materials:** The following monomers were used for thiol-ene polymer synthesis: diallyl terephthalate (DATP, 98% TCI EUROPE N.V.) as diene, glycol dimercaptoacetate (GDMA, 95% Bruno Bock Chemische Fabrik GmbH & Co.) as dithiol, and trimethylolpropane tris(3-mercaptopropionate) (TMPMP, 95% Bruno Bock Chemische Fabrik GmbH & Co.) as trithiol. Their chemical structure is shown in **Scheme 1**. For colloidal stabilization, alkyldiphenyloxide disulfonate (Dowfax 2A1 45% in water, Aldrich) surfactant was used, whereas hexadecane (HD, Aldrich) co-stabilizer was used to protect the system against the Ostwald ripening process. Initiator 2,2-azobis (2-methylpropionitril) (AIBN, Sigma-Aldrich) was used to initiate the step growth polymerization.



**Scheme 1.** Chemical structures of GDMA, DATP, and TMPMP.

The polymer system was joined with reduced graphene oxide (rGO) obtained by reduction of GO in aqueous dispersion with a concentration of  $10 \text{ mg mL}^{-1}$  (Graphenea) using hydrazine monohydrate (Sigma-Aldrich). Polyvinyl pyrrolidone was added to the dispersion as a colloidal stabilizer (PVP,  $M = 10\,000 \text{ g mol}^{-1}$ , Aldrich) to prevent platelet aggregation due to increased hydrophobicity during reduction.

**Methods—rGO Synthesis:** The preparation of rGO was carried out in a few steps. The first 100 mL of GO was stirred and sonicated in an ice bath for 1 h with a 0.5 s cycle and 70% amplitude using the Hielscher Sonicator-UIS250v (Hielscher Ultrasonics GmbH, Teltow, Germany) in order to break re-aggregated GO platelets during storage. Afterward, 2 wt% of PVP previously dissolved in a small amount of Milli-Q was added into dispersions. The third step was to introduce the dispersion in a reactor that was heated to  $60 \text{ }^\circ\text{C}$ , followed by the addition of 0.2 mL of the reducing agent hydrazine monohydrate (GO: hydrazine monohydrate ratio was 5:1) under continuous stirring for 2 h. The last step was the dialysis of the dispersion for 2 weeks to eliminate the reaction products and excess PVP using a pre-wetted RC tubing dialysis membrane with a molecular weight cutoff of 1 kD.

**Methods—Composite Synthesis:** The nanocomposite systems were synthesized via in situ miniemulsion polymerization, where a monomer mixture of DATP, GDMA, and TMPMP was polymerized in the presence of different quantities of rGO (0.2–1 wt% with respect to monomers). To obtain high conversion and higher molar masses, it is necessary to ensure the stoichiometric balance of the ene and thiol functional groups. As trithiol TMPMP was added to the formulation (20 wt% of the total thiol amount), the resulting polymers were cross-linked. The organic phase, composed of monomers, initiator, and costabilizer hexadecane, was added to the aqueous phase made of surfactant (Dowfax 2A1), rGO stabilized by PVP, and Milli-Q. The miniemulsion was prepared by sonication of the coarse emulsion obtained by mixing the aqueous and organic phases. The sonication was performed in an ice bath using a Branson 450 Digital Sonifier (Branson Ultrasonics Corporation, Mexico) with an efficient time of 10 min (0.5 s on and 1 s off) and an amplitude of 70%. The composition of the systems with 30% solids content is given in Table S1, Supporting Information.

The casting technique was used for the formation of the composite films. To obtain films with a thickness of 0.5 mm, a particular amount of the hybrids was cast into silicon molds with dimensions of  $5 \times 3 \text{ cm}$  and left to dry for 5 days under atmospheric conditions ( $25 \text{ }^\circ\text{C}$  and 50% relative humidity).

**Characterization:** The average particle diameter of the hybrids was measured using dynamic light scattering (Zetasizer Nano Z, Malvern Instruments). Before the analysis, the samples were diluted with deionized water to avoid multiple scatterings. The represented value was obtained as an average of three repeated measurements.

The morphology of the nanocomposite films was determined using scanning electron microscopy (SEM; Quanta 250 e-SEM, Philips Tecnaï, field emission, Schottky filaments). The samples were scanned without sputtering with metal. For cross-section imaging, the samples were fractured after being immersed in liquid nitrogen. Transmission electron microscopy (TEM, Philips TECNAI G2 20 TWIN) was used in order to examine the structure of the samples. The samples had a thickness of  $\approx 80 \text{ nm}$

obtained at  $-40\text{ }^{\circ}\text{C}$  using a cryomicrotome device (Leica EMFC6) equipped with a diamond knife. The ultrathin sections were placed on 300-mesh copper grids.

Non-isothermal differential scanning calorimetry (DSC, Q1000, TA Instruments) was used to determine the thermal characteristics of the films. The DSC samples were prepared by placing 10 mg of film in an aluminum crucible and sealing it with an aluminum lid. Three cycles were performed. The samples were heated up to  $150\text{ }^{\circ}\text{C}$  at  $10\text{ }^{\circ}\text{C min}^{-1}$ . They were then cooled at  $10\text{ }^{\circ}\text{C min}^{-1}$  until  $-70\text{ }^{\circ}\text{C}$  and subsequently heated to  $150\text{ }^{\circ}\text{C}$  at  $10\text{ }^{\circ}\text{C min}^{-1}$ .

The mechanical properties of the composite films were evaluated using the TA.HD Plus texture analyzer (Stable Micro Systems Ltd., Godalming, UK). Flat “dog-bone”-shaped tensile test specimens with dimensions of  $15\text{ mm} \times 3.5\text{ mm} \times 0.5\text{ mm}$  were cut from the dry films. The stress-strain measurements were taken under a constant strain velocity of  $1.5\text{ mm s}^{-1}$  and a nominal strain rate of 0.1 Hz. Five (5) specimens were prepared from each sample, and the values presented are the average of five measurements.

To determine the water uptake, a small piece of the film was weighed ( $m_0$ ) and immersed in distilled water at room temperature. Then, it was taken out of the water at given times, dried with an adsorbent paper, weighed ( $m_t$ ), and placed again in the distilled water. The water uptake was calculated by Equation (1):

$$\text{Water uptake (\%)} = \frac{m_t - m_0}{m_0} \times 100 \quad (1)$$

For humidity sensing performance measurements, a handcrafted device was utilized consisting of oxidized silicon wafers equipped with interdigitated gold electrode structures (75 finger pairs,  $3150\text{ }\mu\text{m}$  width and  $2000\text{ }\mu\text{m}$  height,  $10\text{ }\mu\text{m}$  spacing,  $1800\text{ }\mu\text{m}$  overlap; IESM, TU Freiberg). The following steps were involved in the preparation of the samples: First, the emulsions were homogenized in an ultrasonic bath (SONOREX SUPER 10 P, Bandelin, Germany) for 30 min with a power of 10%. Then the samples were coated on the oxidized silicon wafers equipped with interdigitated gold electrode structures using a spin coater (Delta 10, BLE Laboratory Equipment GmbH, Singen, Germany) with speeds of 500 rpm for 40 s, and then the speed was increased to 3500 rpm for 6 s. The coated electrodes were left for 24 h at room temperature to dry, and after that, their conductivity was measured using a digital multimeter Voltcraft VC870 in purified and dried air as carrier gas. To investigate the selectivity of the sensor materials, four vapors that have similar vapor pressures were used: toluene ( $\epsilon = 2.38$ ), 4-methyl-2-pentanone (4M2P,  $\epsilon = 13.1$ ), 1-propanol ( $\epsilon = 20.8$ ), and water ( $\epsilon = 80.1$ ). The polarity and structural features have an important influence on the partitioning of the analyte in the sensor coating. Room temperature and an applied bias of 100 mV were used to monitor the resistance of the sensor. The sensor's response is represented as a change in resistance,  $\Delta R$ .

## Supporting Information

Supporting Information is available from the Wiley Online Library or from the author.

## Acknowledgements

The authors would like to acknowledge the financial support obtained from NATO Science for Peace Program (G6011), M-ERA.NET Network (PCI2022-132934) and from the Basque Government through grant IT1503-22.

## Conflict of Interest

The authors declare no conflict of interest.

## Data Availability Statement

The data that support the findings of this study are available on request from the corresponding author. The data are not publicly available due to privacy or ethical restrictions.

## Keywords

hybrid latex, reduce graphene oxide, resistive sensor, thiol-ene polymers, water vapors detection

Received: January 23, 2024

Revised: May 4, 2024

Published online:

- [1] Y. Li, M. J. Yang, Y. She, *Talanta* **2004**, *62*, 707.
- [2] D. Jung, J. Kim, G. S. Lee, *Sens. Actuators, A* **2015**, *223*, 11.
- [3] V. I. Popov, D. V. Nikolaev, V. B. Timofeev, S. A. Smagulova, I. V. Antonova, *Nanotechnology* **2017**, *28*, 355501.
- [4] X. Leng, D. Luo, Z. Xu, F. Wang, *Sens. Actuators, B* **2018**, *257*, 372.
- [5] N. Li, X. Chen, X. Chen, X. Ding, X. Zhao, *RSC Adv.* **2017**, *7*, 45988.
- [6] G. Hassan, M. Sajid, C. Choi, *Sci. Rep.* **2019**, *9*, 15227.
- [7] H. Bi, K. Yin, X. Xie, J. Ji, S. Wan, L. Sun, M. Terrones, M. S. Dresselhaus, *Sci. Rep.* **2013**, *3*, 2714.
- [8] W. Yao, X. Chen, J. Zhang, *Sens. Actuators, B* **2010**, *145*, 327.
- [9] J. Boudaden, M. Steinmaß, H. E. Endres, A. Drost, I. Eisele, C. Kutter, P. Müller-Buschbaum, *Sensors* **2018**, *18*, 1516.
- [10] B. Chachulski, J. Gebicki, G. Jasinski, P. Jasinski, A. Nowakowski, *Meas. Sci. Technol.* **2006**, *17*, 12.
- [11] M. Myers, J. Cooper, B. Pejčić, M. Baker, B. Raguse, L. Wiczorek, *Sens. Actuators, B* **2011**, *155*, 154.
- [12] L. J. Hubble, J. S. Cooper, A. Sosa-Pintos, H. Kiiveri, E. Chow, M. S. Webster, L. Wiczorek, B. Raguse, *ACS Comb. Sci.* **2015**, *17*, 120.
- [13] W. Zhang, R. Wang, Q. Zhang, J. Li, *J. Phys. Chem. Solids* **2012**, *73*, 517.
- [14] P. G. Su, H. C. Hsu, C. Y. Liu, *Sens. Actuators, B* **2013**, *178*, 289.
- [15] I. Fratoddi, A. Bearzotti, I. Venditti, C. Cametti, M. V. Russo, *Sens. Actuators, B* **2016**, *225*, 96.
- [16] J. Majewski, *Prz. Elektrotech.* **2016**, *1*, 76.
- [17] M. M. Y. Sakai, Y. Sadaoka, *Sens. Actuators, B* **1996**, *36*, 85.
- [18] W. De Lin, H. M. Chang, R. J. Wu, *Sens. Actuators, B* **2013**, *181*, 326.
- [19] T. Fei, K. Jiang, S. Liu, T. Zhang, *Sens. Actuators, B* **2014**, *190*, 523.
- [20] T. Fei, K. Jiang, F. Jiang, R. Mu, T. Zhang, *J. Appl. Polym. Sci.* **2014**, *131*, 1.
- [21] U. Kalsoom, S. Waheed, B. Paull, *ACS Appl. Mater. Interfaces* **2020**, *12*, 4962.
- [22] R. Najjar, S. Nematdoust, *RSC Adv.* **2016**, *6*, 112129.
- [23] H. W. Yu, H. K. Kim, T. Kim, K. M. Bae, S. M. Seo, J. M. Kim, T. J. Kang, Y. H. Kim, *ACS Appl. Mater. Interfaces* **2014**, *6*, 8320.
- [24] W. Li, F. Xu, L. Sun, W. Liu, Y. Qiu, *Sens. Actuators, B* **2016**, *230*, 528.
- [25] Y. Li, T. Wu, M. Yang, *Sens. Actuators, B* **2014**, *203*, 63.
- [26] C. Chen, X. Wang, M. Li, Y. Fan, R. Sun, *Sens. Actuators, B* **2018**, *255*, 1569.
- [27] R. Liang, A. Luo, Z. Zhang, Z. Li, C. Han, W. Wu, *Sensors* **2020**, *20*, 5601.
- [28] S. Borini, R. White, D. Wei, M. Astley, S. Haque, E. Spigone, N. Harris, *ACS Nano* **2013**, *7*, 11166.
- [29] C. Lv, C. Hu, J. Luo, S. Liu, Y. Qiao, Z. Zhang, J. Song, Y. Shi, J. Cai, A. Watanabe, *Nanomaterials* **2019**, *9*, 422.
- [30] J. Boudaden, M. Steinmaß, H. E. Endres, A. Drost, I. Eisele, C. Kutter, P. Müller-Buschbaum, *Sensors* **2018**, *18*, 1516.

- [31] A. B. Çiğil, H. Cankurtaran, M. V. Kahraman, *React. Funct. Polym.* **2017**, *114*, 75.
- [32] M. Ehsani, P. Rahimi, Y. Joseph, *Sensors* **2021**, *21*, 3291.
- [33] A. Trajcheva, N. Politakos, B. T. Pérez, Y. Joseph, J. Blazevska Gilev, R. Tomovska, *Polymer* **2021**, *213*, 123335.
- [34] A. Arzac, G. P. Leal, R. Fajgar, R. Tomovska, *Part Part Syst Charact* **2014**, *31*, 143.
- [35] B. T. Pérez-Martínez, L. Farías-Cepeda, V. M. Ovando-Medina, J. M. Asua, L. Rosales-Marines, R. Tomovska, *Beilstein J. Nanotechnol.* **2017**, *8*, 1328.
- [36] A. Arzac, G. P. Leal, J. C. de la Cal, R. Tomovska, *Macromol. Mater. Eng.* **2017**, *302*, 1600315.
- [37] N. B. Cramer, T. Davies, A. K. O'Brien, C. N. Bowman, *Macromolecules* **2003**, *36*, 4631.
- [38] C. E. Hoyle, T. Y. Lee, T. Roper, *J. Polym. Sci. A Polym. Chem.* **2004**, *42*, 5301.
- [39] F. Jasinski, E. Lobry, B. Tarablsi, A. Chemtob, C. Croutxé-Barghorn, D. Le Nouen, A. Criqui, *ACS Macro Lett.* **2014**, *3*, 958.
- [40] D. H. Do, M. Ecker, W. E. Voit, *ACS Omega* **2017**, *2*, 4604.
- [41] C. M. Q. Le, G. Schrodj, I. Ndao, B. Bessif, B. Heck, T. Pfohl, G. Reiter, J. Elgoyhen, R. Tomovska, A. Chemtob, *Macromol. Rapid Commun.* **2022**, *43*, 2100740.
- [42] M. Argaziz, F. Ruip, M. Aguirre, R. Tomovska, *Polymers*, **2020**, *1*, 3098.
- [43] S. Guo, Y. Lu, B. Wang, C. Shen, J. Chen, G. Reiter, B. Zhang, *Soft Matter* **2019**, *15*, 2981.
- [44] B. Jiang, J. G. Tsavalas, D. C. Sundberg, *Prog. Org. Coat.* **2017**, *105*, 56.
- [45] C. M. Q. Le, G. Schrodj, I. Ndao, B. Bessif, B. Heck, T. Pfohl, G. Reiter, J. Elgoyhen, R. Tomovska, A. Chemtob, *Macromol. Rapid Commun.* **2022**, *43*, 2100740.
- [46] H. Dai, N. Feng, J. Li, J. Zhang, W. Li, *Sens. Actuators, B* **2019**, *283*, 786.